



Simulations of soluble surfactants in 3D multiphase flow



Metin Muradoglu^{a,*}, Gretar Tryggvason^{b,2}

^a Department of Mechanical Engineering, Koc University, Rumelifeneri Yolu, Sariyer, 34450 Istanbul, Turkey

^b Department of Aerospace and Mechanical Engineering, The University of Notre Dame, Notre Dame, IN, United States

ARTICLE INFO

Article history:

Received 12 February 2014

Received in revised form 6 June 2014

Accepted 12 June 2014

Available online 30 June 2014

Keywords:

Soluble surfactant

Front-tracking method

Multi-phase flows

Marangoni effects

Buoyancy-driven flow

Pressure-driven flow

ABSTRACT

A finite-difference/front-tracking method is developed for simulations of soluble surfactants in 3D multiphase flows. The interfacial and bulk surfactant concentration evolution equations are solved fully coupled with the incompressible Navier–Stokes equations. A non-linear equation of state is used to relate interfacial surface tension to surfactant concentration at the interface. Simple test cases are designed to validate different parts of the numerical algorithm and the computational results are found to be in a good agreement with the analytical solutions. The numerical algorithm is parallelized using a domain-decomposition method. It is then applied to study the effects of soluble surfactants on the motion of buoyancy-driven bubbles in a straight square channel in nearly undeformable (spherical) and deformable (ellipsoidal) regimes. Finally the method is used to examine the effects of soluble surfactants on the lateral migration of bubbles in a pressure-driven channel flow. It is found that surfactant-induced Marangoni stresses counteract the shear-induced lift force and can reverse the lateral bubble migration completely, i.e., the contaminated bubble drifts away from the channel wall and stabilizes at the center of the channel when the surfactant-induced Marangoni stresses are sufficiently large.

© 2014 Elsevier Inc. All rights reserved.

1. Introduction

The presence of surface active agents (surfactants) can critically alter the dynamics of interfacial flows by changing the surface tension [32,46]. The surfactant molecules are typically composed of hydrophilic heads and hydrophobic tails, and tend to accumulate at the fluid–fluid interfaces as a mono-molecular layer. They interact with the cohesive forces between the fluid molecules, and thus reduce the surface tension and stabilize the interface. Surfactants are widely used to manipulate interfacial flows in many industrial and biomedical applications [44]. Surface tension usually plays a dominant role in microfluidic systems due to a large surface area to volume ratio [45]. Therefore, surfactants are utilized to alter drop dynamics in microchannels [50], and to synthesize micron or submicron size monodispersed drops and bubbles for microfluidic applications [4]. In physiology, pulmonary surfactant reduces the surface tension on the liquid–gas interface and prevents collapse of lung at the end of expiration [19]. Prematurely born neonates may develop respiratory distress syndrome (RDS) as their lungs are not mature enough to produce sufficient amount of surfactant. Surfactant replacement therapy (SRT) is a standard treatment for premature neonates suffering from RDS [25].

* Corresponding author.

E-mail addresses: mmuradoglu@ku.edu.tr (M. Muradoglu), gtryggva@nd.edu (G. Tryggvason).

¹ Tel.: +90 (212)338 14 73; fax: +90 (212)338 15 48.

² Tel.: +1 (574)631 71 48; fax: +1 (574)631 83 41.

Surfactant physics is extremely complicated: surfactants usually behave differently when the surface is saturated and when it is not, several surfactant phases may exist and they may form a plastic shell that is partly undeformable. Unlike insoluble surfactant that can be present only at the interface, soluble surfactant exists at the interface and in one or both fluid phases [43]. Surfactant is adsorbed from the bulk fluid onto the interface and is desorbed back into the bulk fluid when the interfacial concentration exceeds the equilibrium value. Surface tension is modified only by the interfacial surfactant concentration. The evolution of the surfactant concentration at the interface and in the bulk fluid is typically described by two separate transport equations and the surface tension is related to the interfacial surfactant concentration by an equation of state. The interfacial and bulk surfactant concentration evolution equations are coupled through the surfactant mass flux between the bulk fluid and the interface.

Computational modeling of soluble surfactants in multiphase flows is a challenging task. The bulk and interfacial surfactant evolution equations must be solved fully coupled with the flow equation. In particular, the interfacial transport equation must be solved on moving and deforming interfaces that may also undergo topological changes through breakup and coalescence. The interfacial surfactant concentration alters the surface tension locally. A non-uniform distribution of surfactant at the interface creates Marangoni stresses, which in turn influences the flow field in a complicated way. Meanwhile the flow field alters the surfactant concentration both at the interface and in the bulk fluid. These interactions are highly complicated and non-linear. In addition, the bulk concentration varies discontinuously at the interface when the surfactant is soluble only in one phase. Thus conventional central differences cause oscillations in the bulk surfactant concentration near the interface while low-order one-sided differences are excessively dissipative.

Early computational studies on the effects of surfactants were confined to Stokes flow using a boundary integral method [13,48,57]. The boundary integral method employs a surface mesh to track the interface. Stone and Leal [48] developed a boundary element method and investigated the effects of insoluble surfactants on the deformation and breakup of drops. This method has been extended to large viscosity ratios by Milleken et al. [36], to full 3D flows by Li and Pozrikidis [31] and to soluble surfactant by Milliken and Leal [37]. More recently, Johnson and Borhan [24] used the boundary integral method to study effects of surfactant solubility on motion of surfactant-laden drops in pressure-driven flow through cylindrical capillaries. A comprehensive review of the method can be found in [41].

In recent years, a number of numerical schemes based on popular interface capturing/tracking methods have been developed for direct simulations of interfacial flows with insoluble surfactant such as volume-of-fluid (VOF) [5,11,21], level set [60,61], arbitrary Lagrangian–Eulerian method [17,42], immersed boundary method [28], diffuse interface method [54], segmented projection method (SPM) [27] and smoothed particle hydrodynamics (SPH) [3]. Treatment of insoluble surfactant is relatively easy compared to the soluble surfactant since adsorption of mass to, and desorption of mass from, the interfaces pose a major challenge for the numerical algorithms. This is particularly true for the front-tracking method since the interface is represented by a Lagrangian grid [55].

Surfactant solubility plays a major role in a wide range of applications. Simplifying assumptions were generally made in the early treatment of soluble surfactants. For instance, Stebe et al. [12,23] assumed that the adsorption and desorption of surfactant from the bulk is diffusion dominated so the bulk surfactant concentration remains constant. The most recent research efforts have been directed towards the development of computational methods for direct numerical simulation of interfacial flows with soluble surfactant. Muradoglu and Tryggvason [38] developed a front-tracking method for simulation of soluble surfactant in 2D (axisymmetric) multiphase flows. This method has been successfully applied to various interfacial flows of practical interest [39,40,53]. A similar front-tracking method has also been proposed by Zhang et al. [63] for simulation of a deformable bubble moving through a cylindrical tube in the presence of soluble or insoluble surfactants. This method has been also applied to study effect of a soluble surfactant on a finite-sized bubble motion in a blood vessel [49]. Liu and Zhang [33] have developed a phase-field method and applied it to examine the effects of soluble surfactant on 2D droplet deformation, breakup and coalescence. Adami et al. [3] have developed a smoothed particle hydrodynamics (SPH) method for simulations of insoluble and soluble surfactants in 2D interfacial flows. Teigen et al. [54] have proposed a diffuse-interface method and presented results for 2D and 3D drop deformation in shear flow with soluble surfactant. Ganesan and Tobishka [18] have developed a finite-element scheme based on a coupled arbitrary Lagrangian–Eulerian and Lagrangian approach for the computation of 2D (axisymmetric) interfacial flows with soluble surfactant. They presented simulation results for the effects of surfactant on the buoyancy-driven motion of bubbles. Fujioka [15] has recently proposed a particle method based on the moving particle semi-implicit (MPS) approach for simulations of soluble surfactants in 2D multiphase flows. Khatri and Tornberg [26] have extended their segmented projection method (SPM) [27] to treat soluble surfactant in 2D multiphase flows. Booty and Siegel [6] have proposed a hybrid method for efficient simulation of soluble surfactants in multiphase flows at high Peclet numbers.

In this paper, we present a front-tracking method for direct simulation of soluble surfactant in 3D multiphase flows. The method is designed to solve both the bulk and interface concentration equations fully coupled with the incompressible Newtonian flow equations. Following Muradoglu and Tryggvason [38], the mass transfer between the bulk fluid and the interface is modeled in a conservative manner by distributing the amount of surfactant adsorbed by the interface as a negative source term for the bulk concentration equation near the interface using a distribution scheme widely used in front-tracking methods [55]. A fifth order WENO-Z [7] scheme is used to discretize the convective terms in the bulk surfactant concentration equation. A QUICK scheme is used to approximate the convective terms in the momentum equations. All other spatial derivatives are approximated using second order central differences. Time integration is achieved using a second order predictor–corrector method. Simple test cases are designed to validate the various parts of the numerical

method and the results are found to be in a good agreement with analytical solutions. The numerical algorithm is parallelized using a domain decomposition technique. The method is then applied to study the effects of a surfactant on the motion and deformation of a buoyancy-driven bubble rising in a straight square tube. Both nearly undeformable (spherical) and deformable (ellipsoidal) regimes are considered. Finally, the method is used to simulate the effects of surfactant on the lateral migration of a bubble in a pressure-driven channel flow at moderate Reynolds number, i.e., $Re = 1000$. This is the problem studied experimentally by Takagi et al. [51] and computationally by Fukuta et al. [16]. It is found that the surfactant induced Marangoni stresses can dominate over the shear-induced lift force and thus alter the behavior of the bubble completely, i.e., the contaminated bubble drifts away from the channel wall and stabilizes at the center of the channel in contrast with the corresponding clean bubble that drifts toward the wall and stabilizes near the wall. The grid convergence and second order accuracy of the method have been demonstrated through comprehensive simulations for this problem.

In the next section, the governing equations are described for multiphase flows with soluble surfactants. The numerical algorithm is presented in Section 3. The accuracy of the numerical algorithm is demonstrated in Section 4 using simple test cases for which analytical solutions are available. Some computational examples are presented and discussed in Section 5 and finally conclusions are drawn in Section 6.

2. Governing equations

The flow equations are described here in the context of the finite-difference/front-tracking (FD/FT) method. We assume that the flow in both phases is governed by the incompressible Navier–Stokes equations. Following Unverdi and Tryggvason [58], a single set of governing equations can be written for the entire computational domain as long as the jumps in material properties such as density, viscosity and molecular diffusion coefficient are correctly accounted for and surface tension is included. The Navier–Stokes equations in conservative form are then given by

$$\frac{\partial \rho \mathbf{u}}{\partial t} + \nabla \cdot (\rho \mathbf{u} \mathbf{u}) = -\nabla p + \nabla \cdot \mu (\nabla \mathbf{u} + \nabla \mathbf{u}^T) + \int_A \sigma(\Gamma) \kappa \mathbf{n} \delta(\mathbf{x} - \mathbf{x}_f) dA, \tag{1}$$

where \mathbf{u} is the velocity, p is the pressure, and ρ and μ are the discontinuous density and viscosity fields, respectively. The effects of surface tension are included as a body force in the last term on the right hand side, where σ is the surface tension that is function of the surfactant concentration Γ at the interface, κ is twice the mean curvature, and \mathbf{n} is a unit vector normal to the interface. The surface tension acts only on the interface as indicated by the three-dimensional delta function δ whose arguments \mathbf{x} and \mathbf{x}_f are the point at which the equation is evaluated and a point at the interface, respectively.

The Navier–Stokes equations are supplemented by the incompressibility condition:

$$\nabla \cdot \mathbf{u} = 0. \tag{2}$$

We also assume that the material properties remain constant following a fluid particle, i.e.,

$$\frac{D\rho}{Dt} = 0; \quad \frac{D\mu}{Dt} = 0, \tag{3}$$

where D/Dt is the material derivative. The density and viscosity vary discontinuously across the fluid interface and are given by

$$\begin{aligned} \rho &= \rho_o I(\mathbf{x}, t) + \rho_i (1 - I(\mathbf{x}, t)), \\ \mu &= \mu_o I(\mathbf{x}, t) + \mu_i (1 - I(\mathbf{x}, t)), \end{aligned} \tag{4}$$

where the subscripts “i” and “o” denote the properties of the drop and bulk fluid, respectively, and $I(\mathbf{x}, t)$ is the indicator function defined as

$$I(\mathbf{x}, t) = \begin{cases} 1 & \text{in bulk fluid,} \\ 0 & \text{in bubble fluid.} \end{cases} \tag{5}$$

Concentration of surfactant on the interface, Γ , is defined as

$$\Gamma = \frac{dM_s}{dA}, \tag{6}$$

where M_s is the total mass of surfactant and A is the surface area. The surface tension decreases proportional to the surfactant concentration at the interface according to the equation of state derived from Langmuir adsorption [32]

$$\sigma = \sigma_s + \mathcal{R} T \Gamma_\infty \ln \left(1 - \frac{\Gamma}{\Gamma_\infty} \right), \tag{7}$$

where \mathcal{R} is the ideal gas constant, T is the absolute temperature, σ_s is the surface tension of clean interface and Γ_∞ is the maximum packing concentration. Eq. (7) can also be written as

$$\sigma = \sigma_s \left[1 + \beta_s \ln \left(1 - \frac{\Gamma}{\Gamma_\infty} \right) \right], \quad (8)$$

where $\beta_s = \frac{RT\Gamma_\infty}{\sigma_s}$ is the elasticity number. Eq. (8) provides a good model for low interfacial surfactant concentrations but it deviates significantly as the surfactant concentration increases and results in unphysical negative surface tension in the high surfactant concentration limit. Following Muradoglu and Tryggvason [38], Eq. (8) is slightly modified to avoid negative values of the surface tension as

$$\sigma = \sigma_s \left[\max \left(\epsilon_\sigma, 1 + \beta_s \ln \left(1 - \frac{\Gamma}{\Gamma_\infty} \right) \right) \right], \quad (9)$$

where ϵ_σ is taken as 0.05 in the present study. The surfactant concentration Γ evolves by [47]

$$\frac{\partial \Gamma}{\partial t} + \nabla_s \cdot (\Gamma \mathbf{U}_s) = D_s \nabla_s^2 \Gamma + \dot{S}_\Gamma, \quad (10)$$

where the gradient operator along the interface is defined as

$$\nabla_s = \nabla - \mathbf{n}(\mathbf{n} \cdot \nabla). \quad (11)$$

In Eq. (10), \mathbf{U}_s is the tangential velocity on the interface, D_s is the diffusion coefficient along the interface and \dot{S}_Γ is the source term given by

$$\dot{S}_\Gamma = k_a C_s (\Gamma_\infty - \Gamma) - k_d \Gamma, \quad (12)$$

where k_a and k_d are adsorption and desorption coefficients, respectively, and C_s is the concentration of surfactant in fluid immediately adjacent to the interface. The bulk surfactant concentration C is governed by the advection–diffusion equation in the form

$$\frac{\partial C}{\partial t} + \nabla \cdot (C \mathbf{u}) = \nabla \cdot (D_{co} \nabla C), \quad (13)$$

where the coefficient D_{co} is related to the molecular diffusion coefficient D_c and the indicator function I as

$$D_{co} = D_c I(\mathbf{x}, t). \quad (14)$$

The source term is related to the bulk concentration by [12],

$$\dot{S}_\Gamma = -D_{co}(\mathbf{n} \cdot \nabla C|_{\text{interface}}). \quad (15)$$

Following Muradoglu and Tryggvason [38], the boundary condition at the interface given by Eq. (15) is first converted into a source term for the bulk surfactant evolution equation. We assume that all the mass transfer between the interface and bulk takes place in a thin *adsorption* layer adjacent to the interface so that the total amount of mass adsorbed on the interface is distributed over the adsorption layer and added to the bulk concentration evolution equation as a negative source term in a conservative manner. Eq. (13) thus becomes

$$\frac{\partial C}{\partial t} + \nabla \cdot (C \mathbf{u}) = \nabla \cdot (D_{co} \nabla C) + \dot{S}_C, \quad (16)$$

where \dot{S}_C is the source term evaluated at the interface and distributed onto the adsorption layer in a conservative manner.

The governing equations are solved in their dimensional forms but the results are expressed in terms of relevant non-dimensional quantities. Let \mathcal{L} and \mathcal{U} be appropriately defined length and velocity scales, respectively, and $\mathcal{T} = \mathcal{L}/\mathcal{U}$ be the time scale, then governing non-dimensional numbers can be summarized as

$$\begin{aligned} Re &= \frac{\rho_o \mathcal{U} \mathcal{L}}{\mu_o}; & Ca &= \frac{\mu_o \mathcal{U}}{\sigma_s}; & Pe_c &= \frac{\mathcal{U} \mathcal{L}}{D_c}; & Pe_s &= \frac{\mathcal{U} \mathcal{L}}{D_s}; & \frac{\rho_i}{\rho_o}; & \frac{\mu_i}{\mu_o}; \\ k &= \frac{k_a C_\infty}{k_b}; & Bi &= \frac{k_b \mathcal{L}}{\mathcal{U}}; & Da &= \frac{\Gamma_\infty}{\mathcal{L} C_\infty}; & \beta_s &= \frac{RT \Gamma_\infty}{\sigma_s}, \end{aligned} \quad (17)$$

where Re , Ca , Pe_c , Pe_s , k , Bi , Da and β_s are the Reynolds number, the capillary number, the Peclet number based on bulk surfactant diffusivity, the Peclet number based on interface surfactant diffusivity, the dimensionless adsorption depth, Biot number, Damkohler number and the elasticity number, respectively.

3. Numerical method

The flow equations are solved fully coupled with the bulk and interface surfactant concentration evolution equations using an FD/FT method [55,56,58]. In 3D front-tracking method, the interface is represented by an unstructured triangular grid where the interface (or front) consists of points connected by triangular elements. The points only know their coordinates but the elements know about their corner points and the neighboring elements that share their edges [56]. The flow

and bulk surfactant concentration evolution equations are solved on a stretched Cartesian Eulerian grid while the interface concentration evolution equation is solved on the unstructured triangular Lagrangian grid representing the interface. The material properties inside and outside of the drop are set based on the indicator function defined by Eq. (5). The indicator function is computed on the Eulerian grid using the same procedure as described by Tryggvason et al. [55,56].

The Lagrangian grid is also used to compute the surface tension forces on the interface which are then distributed over the neighboring Eulerian grid cells as body forces in a conservative manner [55,58] using Peskin’s distribution function. Since the FD/FT method has been described in details by Unverdi and Tryggvason [58] and reviewed by Tryggvason et al. [55,56] for surfactant-free flows, the basic flow solver is discussed only briefly here for completeness and emphasis is placed on the solution of the bulk and interfacial surfactant concentration evolution equations and coupling with the flow solver.

3.1. Flow solver

The flow equations (Eqs. (1) and (2)) are solved on a stationary staggered Eulerian grid. The spatial derivatives are approximated using second order central finite-differences for all field quantities except for the convective terms that are discretized using a third order QUICK scheme [30]. The time integration is achieved using a projection method first proposed by Chorin [8]. As in Unverdi and Tryggvason [58], Eqs. (1) and (2) are written in the form

$$\frac{\rho^{n+1}\mathbf{u}^{n+1} - \rho^n\mathbf{u}^n}{\Delta t} = \mathbf{A}^n - \nabla p, \tag{18}$$

$$\nabla \cdot \mathbf{u}^{n+1} = 0, \tag{19}$$

where \mathbf{A} is the advective, diffusive and body force terms in Eq. (1). Then the above equation is decomposed as

$$\frac{\rho^{n+1}\mathbf{u}^* - \rho^n\mathbf{u}^n}{\Delta t} = \mathbf{A}^n, \tag{20}$$

$$\frac{\rho^{n+1}\mathbf{u}^{n+1} - \rho^{n+1}\mathbf{u}^*}{\Delta t} = -\nabla p, \tag{21}$$

where \mathbf{u}^* is a provisional velocity ignoring the effect of the pressure. Next the unprojected velocity field is computed from Eq. (20) and then the pressure field is computed as follows: taking the divergence of Eq. (21) and using the incompressibility condition given by Eq. (19), we obtain a non-separable Poisson equation for pressure in the form

$$\nabla \cdot \frac{1}{\rho^{n+1}} \nabla p = -\frac{1}{\Delta t} \nabla \cdot \mathbf{u}^*, \tag{22}$$

which is solved on the Eulerian grid using the parallel semi-coarsening multigrid (PFMG) solver in the HYPRE library [14]. Finally the velocity field at the new time level is computed as

$$\mathbf{u}^{n+1} = \mathbf{u}^* - \frac{\Delta t}{\rho^{n+1}} \nabla p. \tag{23}$$

The above algorithm is only first order accurate in time. Second-order accuracy is recovered by using a simple predictor-corrector scheme in which the first-order solution at $n + 1$ serves as a predictor that is then corrected by the trapezoidal rule as discussed by Tryggvason et al. [55].

3.2. Surfactant concentration at interface

The evolution equation for the interfacial surfactant concentration is solved on the Lagrangian grid. The surfactant concentration is located at the center of triangular front elements representing the average value for each element. Eq. (10) can be expressed as [38],

$$\frac{d\Gamma A}{dt} = AD_s \nabla_s^2 \Gamma + A\dot{S}_\Gamma, \tag{24}$$

where A is the surface area of the interface. Referring to Fig. 1, Eq. (24) can also be written in the integral form for the front element e as,

$$\frac{d}{dt} \iint_{\Delta A_e} \Gamma dA = D_s \iint_{\Delta A_e} \nabla_s^2 \Gamma dA + \iint_{\Delta A_e} \dot{S}_\Gamma dA, \tag{25}$$

where ΔA_e is the surface area of the element. Using a first order explicit Euler scheme, Eq. (25) can be integrated in time to get

$$\frac{(\Gamma \Delta A)_e^{n+1} - (\Gamma \Delta A)_e^n}{\Delta t} = \delta \Gamma_{D_e}^n + (\dot{S}_\Gamma \Delta A)_e^n, \tag{26}$$

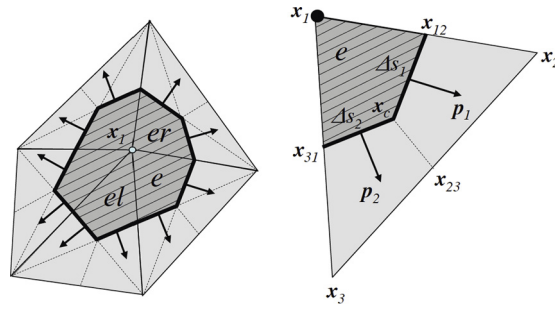


Fig. 1. Computations of surface gradient, surface Laplacian and surface tension force of the 3D front. The surface gradient and surface tension forces are computed at the nodes by adding up contributions from the adjacent elements. The surface Laplacian is computed at cell centers.

where Δt is the time step and $\delta\Gamma_{D_e}^n$ denotes the discrete version of the diffusion term. To evaluate the diffusion term, the area integral is first converted into a line integral using the mathematical identity (see, for instance, Weatherburn [59])

$$\iint_{\Delta A_e} \nabla_s^2 \Gamma dA = \oint_{C_e} \nabla_s \Gamma \cdot \mathbf{p} dl. \tag{27}$$

Here $\mathbf{p} = \mathbf{t} \times \mathbf{n}$, where \mathbf{t} is a vector tangent to the edges of the element and \mathbf{n} is a normal vector to the surface. Then the surface diffusion term is evaluated as

$$\delta\Gamma_{D_e}^n = \left[D_s \iint_{\Delta A_e} \nabla_s^2 \Gamma dA \right]_e^n = \left[D_s \oint_C \nabla_s \Gamma \cdot \mathbf{p} dl \right]_e^n \approx \sum_{k=1}^3 (\nabla_s \Gamma)_k \cdot \mathbf{p}_k \Delta l_k, \tag{28}$$

where Δl_k is the length of k th edge of the front element e and $(\nabla_s \Gamma)_k$ is the surface gradient vector evaluated at the midpoint of k th edge. Surface gradient vector $\nabla_s \Gamma$ is first computed at the element nodes by adding up contributions from the adjacent elements in a similar way as used to compute the curvature [56]. Then the midpoint values are computed by taking simple average of the end point values. The gradient of the surfactant concentration on a curved surface can be evaluated as (see, Weatherburn [59])

$$\nabla_s \Gamma = \lim_{\delta A \rightarrow 0} \frac{1}{\delta A} \oint_C \Gamma \mathbf{p} dl - (\kappa \mathbf{n}) \Gamma, \tag{29}$$

where κ is the mean curvature that has been already computed at the nodes to evaluate the surface tension [56]. The first term on the right hand side of Eq. (29) is evaluated along the thick curve in Fig. 1 as

$$\lim_{\delta A \rightarrow 0} \frac{1}{\delta A} \oint_C \Gamma \mathbf{p} dl \approx \frac{1}{\Delta A} \sum_{ne} \int_{\Delta C_{ne}} \Gamma \mathbf{p} dl, \tag{30}$$

where ΔA denotes the area enclosed by the curve, i.e., the shaded area in the sketch, ΔC_{ne} is the piece of curve in element ne and the summation is carried out over all the neighboring elements. For instance, the contribution from element e to node 1 is evaluated as

$$\int_{\Delta C_e} \Gamma \mathbf{p} dl = \Gamma_1 \mathbf{p}_1 \Delta s_1 + \Gamma_2 \mathbf{p}_2 \Delta s_2, \tag{31}$$

where $\Gamma_1 = (\Gamma_e + \Gamma_{er})/2$, $\Gamma_2 = (\Gamma_e + \Gamma_{el})/2$, $\mathbf{p}_1 = \mathbf{n}_e \times (\mathbf{x}_c - \mathbf{x}_{12})$ and $\mathbf{p}_2 = \mathbf{n}_e \times (\mathbf{x}_{31} - \mathbf{x}_c)$. The midpoints are simply evaluated as average of the end points, e.g., $\mathbf{x}_{12} = (\mathbf{x}_1 + \mathbf{x}_2)/2$. The unit normal vector is computed as

$$\mathbf{n}_e = \frac{\Delta \mathbf{x}_{12} \times \Delta \mathbf{x}_{13}}{|\Delta \mathbf{x}_{12} \times \Delta \mathbf{x}_{13}|}, \tag{32}$$

where $\Delta \mathbf{x}_{12} = (\mathbf{x}_1 - \mathbf{x}_2)$ and so on. Then the curvature term in Eq. (29) is evaluated, for instance, at node 1 as $(\kappa \mathbf{n})_1 \approx (\kappa \mathbf{n})_1 \Gamma_1$. The mean curvature $(\kappa \mathbf{n})_1$ is computed using the same procedure as described by Tryggvason et al. [56] and Γ_1 is computed as a simple average taken over all the front elements sharing node 1. Second-order accuracy is recovered by using the simple predictor–corrector scheme as mentioned in the previous section.

3.3. Bulk surfactant concentration

The bulk surfactant concentration equation is solved on the staggered Eulerian grid following essentially the same procedure developed by Muradoglu and Tryggvason [38] except for the discretization of the convective terms. The bulk surfactant

concentration is located at the pressure nodes. Here the method is briefly described for completeness and the emphasis is placed on the new ingredients.

The spatial derivatives are approximated using second order central differences except for the convective terms. Muradoglu and Tryggvason [38] used a second order ENO scheme to evaluate the convective terms but it is found that the second order ENO scheme is too dissipative in the 3D case. Therefore several discretization schemes have been considered to approximate the convective terms in the present study including second order central and ENO schemes, a third order QUICK and various versions of fifth order upwinded WENO schemes. It is emphasized here that unwinding is needed to avoid excessive oscillations in all the WENO schemes. As discussed in the results section, we found that the central differences and QUICK scheme produce excessive oscillations near the interface while low order one-sided schemes are too dissipative. Of various fifth order WENO schemes considered here, the mapped WENO [20] and WENO-Z [7] schemes are found to be the least dissipative and yield smooth solutions without any excessive oscillations. The upwinded WENO-Z scheme is preferred in the present study mainly due to its simplicity compared to the mapped WENO. Time integration is performed using the second order predictor–corrector scheme [55].

The source term is first computed on the interface and is then distributed over the adsorption layer in a conservative manner [38]. For this purpose, the distribution algorithm is slightly modified as follows: The source term $\dot{S}_{C_{i,j,k}}$ at grid point (i, j, k) is approximated as

$$\dot{S}_{C_{i,j,k}} = - \sum_e \omega_{i,j,k}^e \dot{S}_{r_e} \frac{\Delta A_e}{\Delta V_{i,j,k}}, \tag{33}$$

where \dot{S}_{r_e} is the source term evaluated at the center of the e th element, ΔA_e is the element surface area, $\Delta V_{i,j,k}$ is the volume of the Eulerian grid cell (i, j, k) and $\omega_{i,j,k}^e$ is the weight for the grid point. The weight must satisfy the consistency condition

$$\sum_i \sum_j \sum_k \omega_{i,j,k}^e = 1, \tag{34}$$

in order to conserve the total source strength in going from the interface to the grid. The weight for the grid point (i, j, k) , for smoothing from the center of the e th element (x_f^e, y_f^e, z_f^e) , can be written as

$$\omega_{i,j,k}^k = \frac{\tilde{\omega}_{i,j,k}^e}{\sum_i \sum_j \sum_k \tilde{\omega}_{i,j,k}^e}, \tag{35}$$

where the non-normalized weight function is defined as

$$\tilde{\omega}_{i,j,k}^e = d_c(x_f^e - ih)d_c(y_f^e - jh)d_c(z_f^e - kh). \tag{36}$$

In Eq. (36), the distribution function d_c is a slightly modified version of Peskin’s cosine distribution defined as

$$d_c(x) = \begin{cases} \frac{1}{2h}(1 + \cos(\frac{\pi x}{2h})) & \text{if } |x| < 2h \text{ and } I < 0.5 \\ 0, & \text{otherwise,} \end{cases} \tag{37}$$

where h is the Eulerian grid size. As can be seen in Eq. (37), the source term is distributed only outside of the drop region, i.e., $I(x, y, z, t) \geq 0.5$. Note that, in contrast with the 2D case [38], no special treatment is performed to enforce the boundary condition at the interface since fifth order WENO scheme reduces numerical diffusion substantially compared to the second order ENO scheme used in 2D case.

3.4. Surface tension

Following Tryggvason et al. [56], the surface tension on a surface segment is given by

$$\delta \mathbf{f}_e = \oint_{\Delta C} \sigma(\Gamma) \mathbf{p} dl, \tag{38}$$

where $\sigma(\Gamma)$ is surface tension coefficient evaluated as a function of interfacial surfactant concentration using the equation of state, i.e., Eq. (9). Surface tension is computed at the front element nodes using the same procedure as described by Tryggvason et al. [56]. The surface segment can be selected in different ways and here we select a surface segment consisting of a third of all the elements connected to a given point. The surface segment for the point with coordinates \mathbf{x}_1 is the cross-hatched area, bounded by a thick line, in the left side of Fig. 1. The net contribution to the force on the area segment surrounding point 1, from element e , is the integral over both line segments, so we can write

$$\delta \mathbf{f}_{1e} = \oint_{\Delta C_e} \sigma(\Gamma) \mathbf{p} dl \approx \sigma(\Gamma_1) \mathbf{p}_1 \Delta s_1 + \sigma(\Gamma_2) \mathbf{p}_2 \Delta s_2, \tag{39}$$

where $\Delta s_1 = |\mathbf{x}_{12} - \mathbf{x}_c|$, $\Delta s_2 = |\mathbf{x}_c - \mathbf{x}_{13}|$, $\Gamma_1 = (\Gamma_e + \Gamma_{er})/2$ and $\Gamma_2 = (\Gamma_e + \Gamma_{el})/2$. The contributions from the other elements sharing node 1 are computed in a similar fashion and summed up to find the net force. The surface tension forces computed at the nodes as described above are then distributed onto neighboring Eulerian grid points as a body force in a conservative manner using Peskin's distribution. Details of the distribution can be found in Tryggvason et al. [55,56].

3.5. Overall solution procedure

The finite-difference method is coupled with the front-tracking algorithm following the procedure proposed by Tryggvason et al. [55] and Muradoglu and Tryggvason [38]. In advancing the solutions from time step n to step $n + 1$, first the unprojected velocity field is computed from Eq. (20) and then the marker points are moved for a single time step by

$$\mathbf{X}_p^{n+1} = \mathbf{X}_p^n + \Delta t \mathbf{V}_p^n, \quad (40)$$

where \mathbf{X}_p and \mathbf{V}_p are the positions of the front marker points and the velocity interpolated from the neighboring Eulerian grid nodes onto the front location \mathbf{X}_p using Peskin's distribution, respectively. Next the bulk and interface surfactant concentrations are advanced for a single time step as explained above. Then the material properties are evaluated based on the new locations of the marker points as

$$\rho^{n+1} = \rho(\mathbf{X}_p^{n+1}), \quad \mu^{n+1} = \mu(\mathbf{X}_p^{n+1}), \quad D_{co}^{n+1} = D_{co}(\mathbf{X}_p^{n+1}), \quad \sigma^{n+1} = \sigma(\Gamma^{n+1}). \quad (41)$$

Finally the projected velocity field is computed from Eq. (21).

The time step is restricted to maintain numerical stability. In the present study, the restrictions due to diffusion, convection and surface tension are considered. The time step is given by

$$\Delta t = \alpha_{sf} \min \left(\frac{h_{\min}^2}{6s_{\max}}, \left(\frac{h}{U} \right)_{\min}, \sqrt{\frac{(\rho_o + \rho_i)h_{\min}^3}{4\pi\sigma}} \right), \quad (42)$$

where s_{\max} is the largest value among the kinematic viscosity $\nu = \mu/\rho$ and molecular diffusion coefficient D_c , h_{\min} is the smallest grid size, $(\frac{h}{U})_{\min}$ is the minimum value of grid size h divided by the magnitude of velocity U in the domain. Note that the prefactor α_{sf} in Eq. (42) is the safety factor taken as 0.9 in this study.

The numerical algorithm is parallelized using a domain decomposition method. The message passing interface (MPI) library is used for communication between processors. In the current implementation, the interfaces are assigned to a single processor, i.e., the treatment of interface is not fully parallelized. However, the interface can be readily parallelized for the simulations involving many interfaces.

3.6. Restructuring the Lagrangian grid

In a general flow field, the interface will stretch and deform as a result of the fluid motion. When the interface is stretched, the separation between marker points increases and the elements become too large to resolve the interface adequately. On the other hand, when the interface is compressed, the separation between marker points decreases and the elements become too small compared to the Eulerian grid, which results in unresolved wiggles in the Lagrangian grid in addition to increased computational cost. Therefore the Lagrangian grid is restructured by deleting front elements that are smaller than a prespecified lower limit and splitting front elements that are larger than a prespecified upper limit in the same way as described by Tryggvason et al. [55,56] in order to keep the front-elements nearly uniform. In all the results presented in this paper, the restructuring is performed every 10 time steps. Since the restructuring interface is described in details by Tryggvason et al. [55,56], only the treatment of interfacial surfactant concentration is briefly discussed here. Special attention is paid to conserve the total surfactant mass in deleting and splitting the elements. In refining the grid, the long edge of an element is split to create two new elements as shown in the top sketch of Fig. 2. For instance, after splitting element e_1 , the interfacial surfactant concentration in the daughter cells is set equal to

$$\Gamma_{e_{1nb}} = \Gamma_{e_{1nt}} = \frac{\Delta A_{e_1}}{\Delta A_{e_{1nb}} + \Delta A_{e_{1nt}}} \Gamma_{e_1}, \quad (43)$$

where $\Delta A_{e_{1nb}}$ and $\Delta A_{e_{1nt}}$ are the area of the bottom and top daughter cells, respectively. The total mass is also strictly conserved in deleting elements. For instance, the interfacial surfactant concentration of e_{1n} in the bottom sketch of Fig. 2 is set to

$$\Gamma_{e_{1n}} = \frac{\Delta A_{e_1} \Gamma_{e_1} + \Delta A_{e_{2b}} \Gamma_{e_2}}{\Delta A_{e_{1n}}}, \quad (44)$$

where $\Delta A_{e_{2b}}$ is the area of the lower piece of the element e_2 that becomes part of the element e_{1n} after the deletion.

4. Test cases

Simple test cases are designed to validate the numerical approximations to each term in Eqs. (16) and (25), and the results are compared with the analytical solutions.

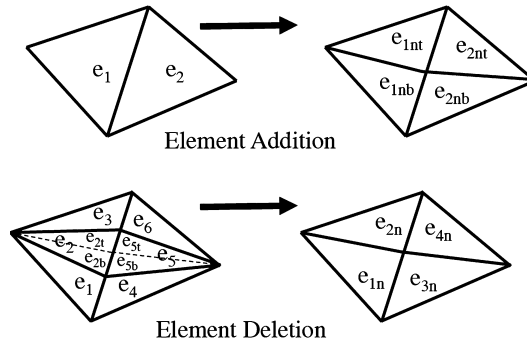


Fig. 2. The restructuring of the front elements. The long edge of an element is split into two daughter elements (top) and the short edge of two elements are collapsed to delete two elements (bottom).

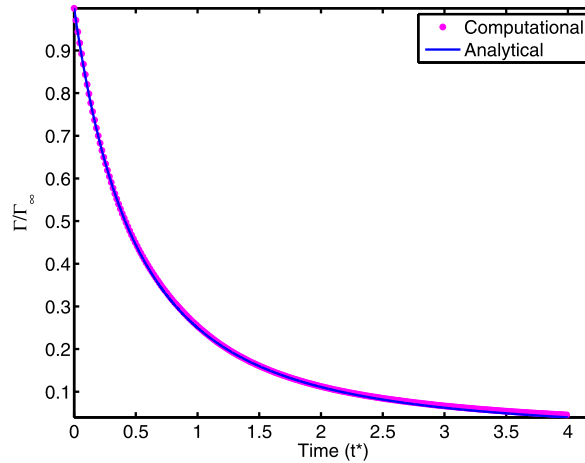


Fig. 3. Advection test: Evolution of surfactant concentration in time for a continuously expanding spherical interface when both the diffusion and source terms are switched off.

4.1. Convection test for the interfacial surfactant

Convection of the interfacial surfactant concentration is quite easy in the front-tracking method mainly due to Lagrangian representation of the interface. However convection also involves restructuring of the interface. Therefore a simple test is performed to validate the numerical approximations to the convective terms in the interfacial surfactant evolution equation and restructuring of the front. For this purpose, we consider a sphere that continuously expands in the normal direction with a constant radial velocity. The initial surfactant concentration is uniform on the sphere. Both the diffusion and the source terms are switched off so that the surfactant concentration changes solely due to the change in the surface area of the drop. For this case, the interfacial surfactant concentration is given by [38]

$$\Gamma^*(t) = \frac{A_0}{A(t)} \Gamma_0^*, \tag{45}$$

where $\Gamma^* = \Gamma/\Gamma_\infty$. In Eq. (45), A_0 and Γ_0^* are the initial surface area and the initial surfactant concentration, respectively. The numerical and analytical solutions for variation of surfactant concentration in time are plotted in Fig. 3. The numerical results are obviously in an excellent agreement with the analytical solution, indicating accurate discretization of the convective terms and consistent treatment of interfacial surfactant concentration in restructuring of the front.

4.2. Interface diffusion test

Computational modeling of the surfactant diffusion on the interface is significantly more difficult in 3D than that in 2D. The test case used by Muradoglu and Tryggvason [38] is adopted here to validate the discretization of the diffusion term in Eq. (10). We consider a stationary spherical interface of radius R and the source term \hat{S}_Γ is switched off. The interfacial surfactant concentration is initialized axi-symmetrically as $\Gamma = \frac{1}{2}(1 - \cos\theta)$ where θ is the polar angle measured from the axis of symmetry. The analytical solution for this problem is given by

$$\Gamma(\theta, t) = \frac{1}{2} \left(1 - e^{-\frac{2t^*}{Pe_s}} \cos\theta \right), \tag{46}$$

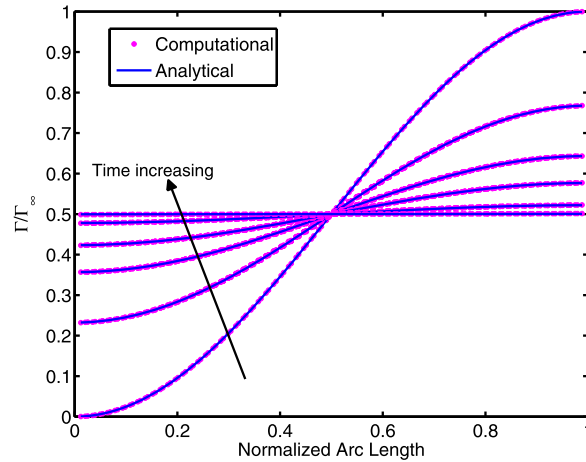


Fig. 4. Surface diffusion test for the interfacial surfactant concentration: The time evolution of the interfacial surfactant concentration for $Pe_s = 10$.

where $Pe_s = \mathcal{U}D/D_s$, $t^* = t\mathcal{U}/R$ and \mathcal{U} is an appropriately defined velocity scale.

The numerical results are compared with the analytical solution in Fig. 4 for $Pe_s = 10$ at various non-dimensional times. As can be seen in this figure, the numerical results match very well with the analytical solution, indicating the accurate discretization of the diffusive terms. Note that the orientation of axis of symmetry with respect to the coordinate system used in the computations is not important, i.e., the axis of symmetry can be any line passing through the center of the sphere. Although not shown here, this test has been repeated for various orientations of the axis of symmetry and the results are found to be essentially the same.

4.3. Test for the Marangoni effects

The next test case deals with the numerical approximation of the surface tension force. Following Muradoglu and Tryggvason [38], we consider a test case that is equivalent to the thermocapillary migration of a viscous drop at vanishing Reynolds and Marangoni numbers studied theoretically by Young et al. [62]. In this test case, a viscous drop of radius R moves solely due to Marangoni stresses in an otherwise quiescent fluid in a channel of a square cross section. The Marangoni stresses are caused by interfacial surfactant concentration specified as a function of the axial coordinate as

$$\frac{\Gamma}{\Gamma_\infty} = z/L_z, \quad (47)$$

where L_z is the channel length in the axial direction. A linear equation of state is used in the form

$$\sigma = \sigma_s \left(1 - \beta_s \frac{\Gamma}{\Gamma_\infty} \right). \quad (48)$$

This test case corresponds to the thermocapillary migration of a viscous drop in a linear ambient temperature gradient and equal heat conductivities of the drop and the continuous fluids. Assuming that the channel size is much larger than the drop size, the steady terminal velocity of the drop is given by [62]

$$V_{YGB} = \frac{2\sigma_s\beta_s R}{L_z(6\mu_o + 9\mu_i)}. \quad (49)$$

We set $\rho_o = \rho_i = 0.2$, $\mu_o = \mu_i = 0.1$, $R = 0.5$ and $\beta_s = 2.0$. Computations are performed for two channel sizes, i.e., $L_x = L_y = 5R$ and $L_x = L_y = 10R$ in order to show the wall effect. The channel height is kept the same at $L_z = 10R$ in both cases. The drop is initially located at the axis and $3R$ above the bottom of the channel. No-slip boundary conditions are used for all boundaries. The computational domain is resolved by uniform grids containing $128 \times 128 \times 256$ and $256 \times 256 \times 256$ cells for the small and larger channels, respectively. The normalized terminal velocity is plotted in Fig. 5 as a function of non-dimensional time and is compared with the analytical solution of Young et al. [62]. It is seen that there is a significant wall effect on the steady state velocity of the droplet as expected due to elliptic nature of low Reynolds number flows. The figure also shows that the drop velocity asymptotically approaches the theoretical results and at the end of the simulation the difference is about 2% for the large channel case. This difference is mainly attributed to the retardation effects of the finite channel size.

4.4. Bulk surfactant convection test

Since the bulk surfactant usually exists only in one phase, the surfactant concentration is discontinuous at the interface. This discontinuity causes a difficulty for the discretization of the convective terms in the bulk surfactant evolution equation.

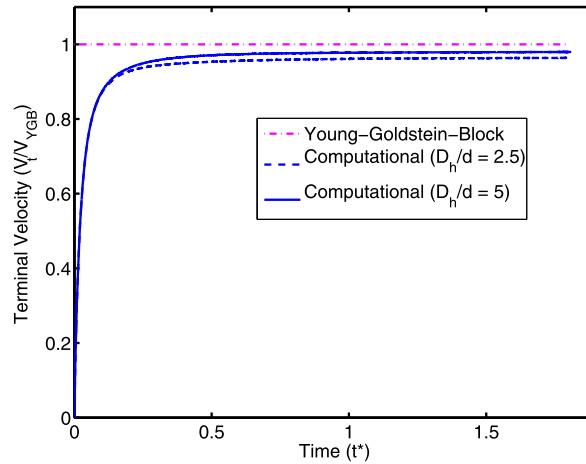


Fig. 5. Marangoni test: Terminal velocity versus time for the Marangoni migration of the droplet with a linear variation of interfacial surface tension in vertical (z) direction. Computations are performed for two sizes of the computational domain to show the effect of finite channel size. The solid and dashed lines are the computational results for the large ($D_h/d = 5$) and the small ($D_h/d = 2.5$) channel, respectively, and dashed-dot line is the theoretical result of Young et al. [62].

The central differences are known to produce excessive oscillations in the vicinity of such discontinuities and low order one-sided schemes are usually too diffusive. A simple test is designed to examine performance of various approaches including the second order ENO, third order QUICK, fifth order WENO of Jiang and Shu (WENO-JS) [22] and fifth order WENO of Borges et al. (WENO-Z) [7] schemes. Test problem deals with the buoyancy-driven rise of a droplet along the axis of a square channel. The channel size is specified as $L_x = 4R$, $L_y = 4R$ and $L_z = 16R$ in x , y and z directions, respectively, where R is the initial drop radius. Boundary conditions are periodic in axial (z) direction while no-slip boundary conditions are applied on the walls in other directions. Eötvös and Morton number are $Eu = 9$ and $Mo = 3.5 \times 10^{-5}$. The density ratio is $\rho_i/\rho_o = 0.1$ and the viscosity ratio is unity. The diffusion and source terms are switched off in the bulk surfactant concentration evolution equation and the interface is clean. Thus the bulk surfactant concentration equation becomes

$$\frac{\partial C}{\partial t} + \nabla \cdot (C\mathbf{u}) = 0. \quad (50)$$

The bulk surfactant concentration along the axis of the channel is plotted in Fig. 6 at various times for QUICK, second order ENO, WENO-JS and WENO-Z schemes. The indicator function is also plotted to mark the location of the interface. The initial surfactant distribution is the same as the indicator function. The plot on the bottom right shows an enlarged version of the plot on the bottom left. This figure shows that the QUICK scheme produces excessive oscillations in the vicinity of the interface while the second order ENO is too dissipative. Although the fifth order WENO-JS is much better than the ENO scheme, it is still more dissipative than the WENO-Z scheme. It is emphasized here that the fifth order mapped WENO scheme of Henrick et al. [20] has been also tested and found to yield about the same result as the WENO-Z scheme. The WENO-Z scheme is preferred here mainly due to its simplicity compared to the mapped WENO scheme. Second order central differences are used near the wall where the solution is smooth in the present study but more elaborate boundary conditions can also be adopted if needed.

4.5. Bulk concentration diffusion and mass transfer test

The final test case is concerned with the diffusion of the bulk concentration and the mass transfer between the bulk and the interface. For this test, we consider a stationary spherical drop of radius R suspended in a large channel. The drop interface is initially clean and the initial bulk surfactant concentration is uniform at $C = C_\infty$. The mass is transferred solely by the molecular diffusion. As in Muradoglu and Tryggvason [38], the source term is simplified as $\dot{S}_r = k_a C_s$ so that the mass transfer is always from the bulk fluid to the interface. For this simplified problem, the surfactant concentration in the bulk fluid evolves by

$$\frac{\partial C}{\partial t} = \frac{D_s}{r^2} \frac{\partial}{\partial r} \left(r^2 \frac{\partial C}{\partial r} \right). \quad (51)$$

An analytical solution to this equation was provided by Muradoglu and Tryggvason [38] in the form

$$\frac{C_\infty - C}{C_\infty} = \frac{k_a \sqrt{\pi D_s t} / D_s}{1 + \frac{\sqrt{\pi D_s t}}{R} \left(1 + \frac{k_a R}{D_s} \right)} \frac{R}{r} \operatorname{erfc} \left(\frac{r - R}{2\sqrt{D_s t}} \right), \quad (52)$$

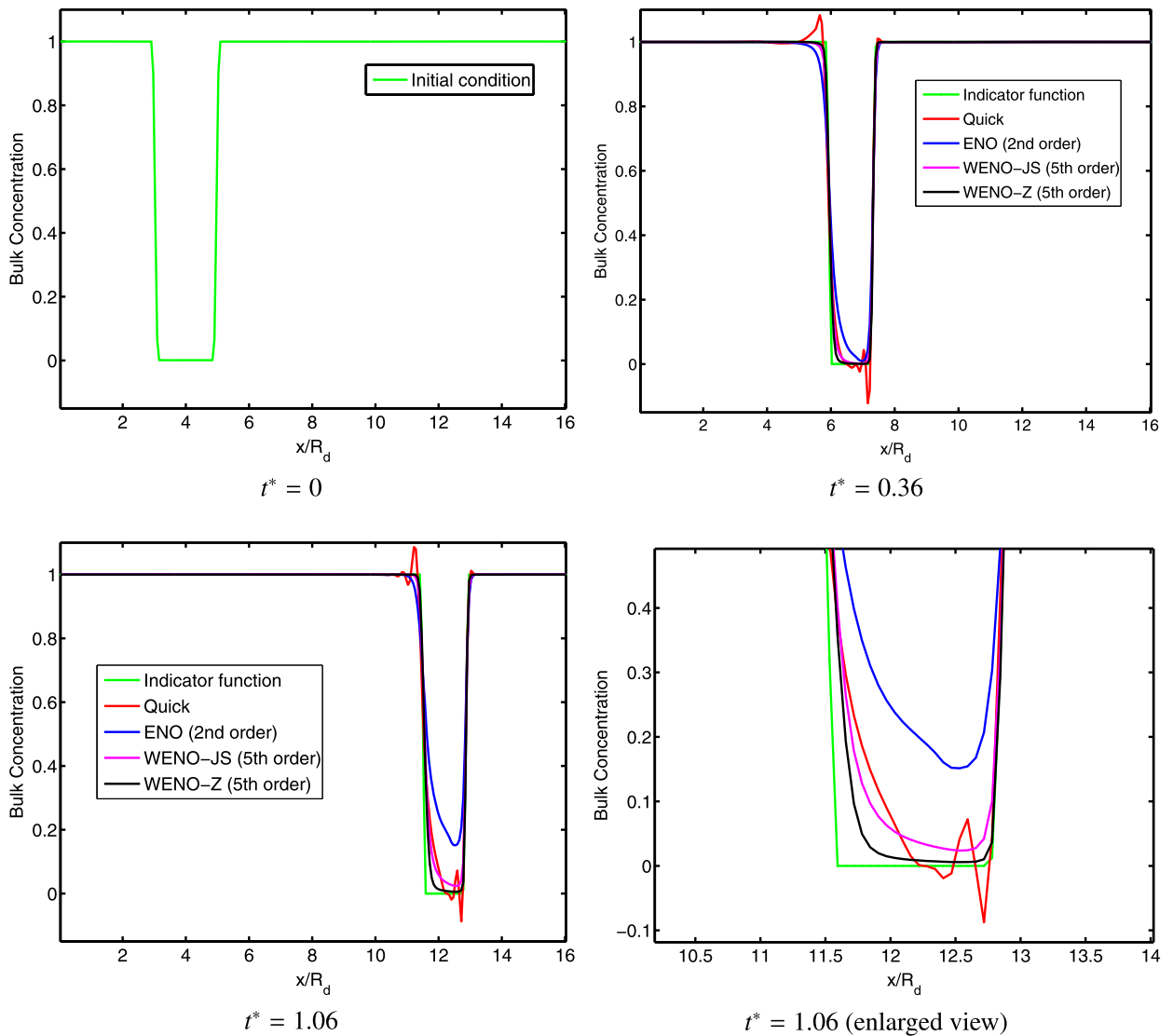


Fig. 6. Bulk convection test: Bulk surfactant concentration at the centerline of the buoyancy-driven bubble at non-dimensional times $t^* = 0, 0.35$ and 1.06 . The diffusion and source terms are switched off in the bulk surfactant concentration evolution equation and the interface is clean. The plot on the right at the bottom shows the enlarged view of the result at $t^* = 1.06$. The indicator function indicates the location of the interface and may be considered as the exact solution.

where $\text{erfc}(x)$ is the complementary error function. However, it has been recently brought to our attention [29] that Eq. (52) is not a correct analytical solution. After a careful examination of our earlier solution, we noticed that the error stemmed from the determination of the integration constants in the similarity solution, i.e., a parameter that had been assumed to be constant in solving the ODE was later determined as a time-dependent variable to satisfy the initial and boundary conditions. In fact, there does not exist any similarity solution for this problem. Nevertheless, it turns out that Eq. (52) is still a very good approximation to the correct solution as discussed below. Eq. (52) is also solved numerically using a finite-difference method. The results are compared both with Eq. (52) and the finite-difference solution.

For this test, a drop of radius R is placed at the center of a cube with side length of $10R$. The computational domain is resolved by a uniform $256 \times 256 \times 256$ Cartesian grid. All quantities are made dimensionless using the length scale $\mathcal{L} = R$ and the time scale $\mathcal{T} = R^2/D_c$. The bulk surfactant profiles are compared with the finite-difference solution and the analytical solution (Eq. (52)) in Fig. 7 at various times. The computational profiles agree well with the finite-difference solution showing the accurate treatment of mass-exchange between bulk and interface. It is also interesting to see that, although not a valid analytical solution, Eq. (52) approximates the correct solution very well, especially at early times.

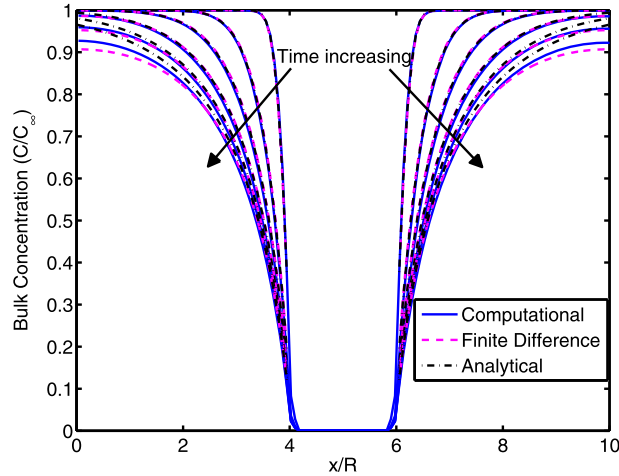


Fig. 7. Bulk surfactant concentration diffusion and mass exchange test: Bulk surfactant concentration profiles at various times. The computational results are compared with the analytical (Eq. (52)) and finite-difference solutions.

5. Computational examples

The different parts of the numerical algorithm have been validated for simple test cases in the previous section. In this section, the method is applied to study the effects of surfactant on the buoyancy-driven motion and deformation of a bubble rising in a straight tube of a square cross-section and on the lateral migration of gas bubble in pressure driven channel flow. The first problem has been studied by Muradoglu and Tryggvason [38] and Tasoglu et al. [53] in axi-symmetric configurations. The second problem is motivated by the recent experimental study by Takagi et al. [51] and computational study by Fukuta et al. [16].

5.1. Buoyancy-driven rising bubbles

We consider a contaminated bubble of radius R rising in a straight tube of square cross-section. The coordinate system is located at the bottom of the channel and the channel centerline is aligned with the z axis. The computational domain is $L_x \times L_y \times L_z$ in x , y and z directions, respectively. Periodic boundary conditions are applied in the axial (z) direction and no-slip boundary conditions are applied on the walls in other directions. The bubble is initially located at the centerline of the channel close to the bottom boundary. The interface is initially clean and the surfactant concentration is uniform in the bulk fluid at $C = C_\infty$. The bubble rises in the channel solely due to density difference between the bubble and the ambient fluids. A buoyancy force, $(\rho - \bar{\rho})\mathbf{g}$, is added to the momentum equation (Eq. (1)). Here $\bar{\rho}$ is the average density of the whole flow domain and $\bar{\rho}\mathbf{g}$ is a hydrostatic force added to keep the net vertical momentum constant.

In addition to the non-dimensional numbers defined in Eq. (17), there are three independent parameters for this problem: the Eötvös number $Eu = \Delta\rho g d / \sigma_s$, the Morton number $Mo = \Delta\rho g \mu_o^4 / \rho_o^2 \sigma_s^3$ and the non-dimensional channel size D_h/d where D_h is the hydraulic diameter of the channel and $d = 2R$. The length and velocity scales are taken as $\mathcal{L} = d$ and $\mathcal{U} = V_{HR}$, respectively, where V_{HR} is the terminal velocity given by Hadamard–Rybczynski solution [9] for a spherical bubble moving in an infinite domain, i.e.,

$$V_{HR} = \frac{2}{3} \frac{g R^2 \Delta\rho}{\mu_o} \frac{\mu_o + \mu_i}{2\mu_o + 3\mu_i}. \quad (53)$$

The time scale is then defined as $\mathcal{T} = \mathcal{L}/\mathcal{U}$. The parameters Pe_c , P_s , Bi and Da are defined based on these scales. However, non-dimensional time (t^*) and Reynolds number (Re) are defined using the actual bubble terminal velocity (V_b) as the velocity scale and $\sqrt{d/g}$ as the time scale.

A nearly spherical bubble is considered first. It is well known that surfactant rigidifies the interface of a nearly spherical bubble and thus the terminal velocity of the bubble reduces significantly [32,53]. This is referred to as the retardation effect of the surfactant. Here, the non-dimensional parameters are $\frac{\rho_i}{\rho_o} = 0.1$, $\frac{\mu_i}{\mu_o} = 0.025$, $Pe_c = 10$, $P_s = 100$, $k = 0.5$, $Da = 0.4$, $Bi = 20$ and $\beta_s = 0.5$. The Eötvös and Morton numbers are $Eu = 1$ and $Mo = 0.1$. Computations are performed for two different non-dimensional channel sizes, i.e., $D_h/d = 2.5$ and $D_h/d = 5$, to show the channel wall effect on the bubble velocity. The evolution of the Reynolds number based on the bubble terminal velocity is plotted in Fig. 8 for the clean and contaminated bubbles rising in a channel with hydraulic diameters of $D_h/d = 2.5$ and $D_h/d = 5$. This figure clearly shows the retardation effect of the surfactant, i.e., the clean bubble continuously accelerates and reaches a steady Reynolds number (or terminal velocity) while the contaminated bubble first accelerates, reaches a peak velocity but then decelerates as the surfactant accumulates at the interface and finally reaches a steady Reynolds number. This observation is consistent with

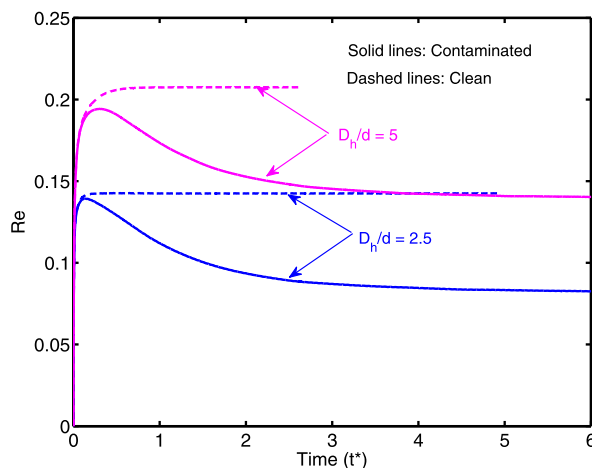


Fig. 8. Reynolds number versus non-dimensional time for a buoyancy-driven contaminated bubble in a nearly spherical regime for the non-dimensional hydraulic channel diameters $D_h/d = 2.5$ and $D_h/d = 5.0$. The dashed and solid lines indicate the clean and contaminated cases, respectively.

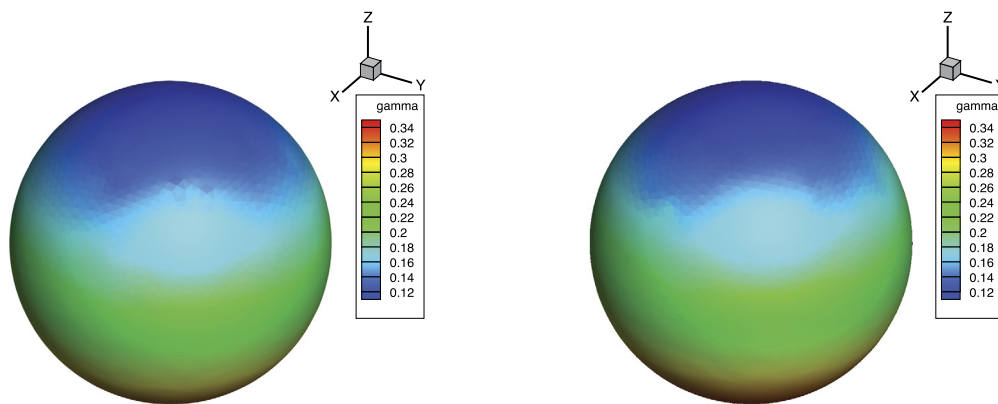


Fig. 9. Distribution of surface concentration on a buoyancy-driven contaminated bubble in a nearly spherical regime at time $t^* = 4.32$ for non-dimensional channel diameters of $D_h/d = 2.5$ (left) and $D_h/d = 5.0$ (right).

experimental observation (see, for instance, Clift et al. [9]) and with the axisymmetric computations of Tasoglu et al. [53]. The constant contours of interfacial surfactant concentration at steady state are plotted in Fig. 9 for $D_h/d = 2.5$ and $D_h/d = 5$ cases. The smooth distribution of interfacial surfactant concentration can be considered as a good indicator of the accuracy of the computational results.

A more deformable (ellipsoidal) bubble is then considered. For this purpose, the Eötvös and Morton numbers are set to $Eu = 10$ and $Mo = 10^{-3}$, respectively. The non-dimensional channel size is chosen as $D_h/d = 2.5$, and the other parameters are $\rho_i/\rho_o = 0.1$, $\mu_i/\mu_o = 0.025$, $Pe_s = 100$, $Pe_s = 100$, $k = 1$, $Da = 0.2$, $Bi = 0.75$ and $\beta_s = 0.5$. The Reynolds number is plotted in Fig. 10 as a function of non-dimensional time for the clean and contaminated bubbles. This figure also shows significant retardation effect of the surfactant but the decrease in terminal velocity is not as dramatic as that in the nearly spherical case. The contours of the constant interfacial surfactant concentration on the bubble at steady state are shown in Fig. 11. As can be seen, the surfactant is swept from the front part and accumulated at the back of the bubble due to strong convection in this case. This result is also consistent with the axisymmetric computations of Tasoglu et al. [53].

5.2. Effects of surfactant on lateral motion of a bubble in pressure-driven channel flow

Finally the method is used to study the effects of soluble surfactant on the lateral migration of a bubble in a pressure-driven channel flow. This problem is motivated by the recent experimental study of Takagi et al. [51]. It is well known that the deformability plays an important role for lateral migration of bubbles in a shear flow: Bubbles with low deformability move toward the wall due to shear-induced lift force and concentrate near the wall while bubbles with high deformability migrate toward the center of the channel and concentrate at the channel center [10,34,35]. Takagi et al. [51] have recently demonstrated that small amount of surfactant can drastically change the bubble behavior and reverse the direction of lateral bubble migration in shear flow. They have shown that these influences can cause a drastic change in the whole bubbly flow structure [51,52]. Fukuta et al. [16] performed a computational study to examine the effects of soluble surfactant on lateral

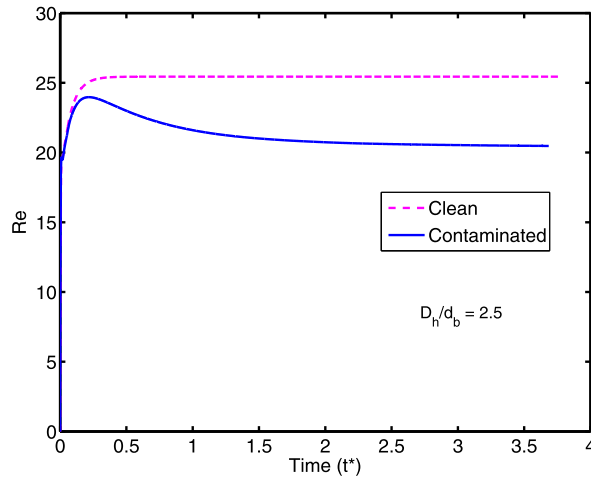


Fig. 10. Reynolds number versus non-dimensional time for the buoyancy-driven contaminated bubble in an ellipsoidal regime. ($Eo = 10$, $Mo = 0.001$, $Pe_s = Pe_c = 1000$, $k = 1$, $Da = 10$, $Bi = 0.075$ and $D_h/d_b = 2.5$).

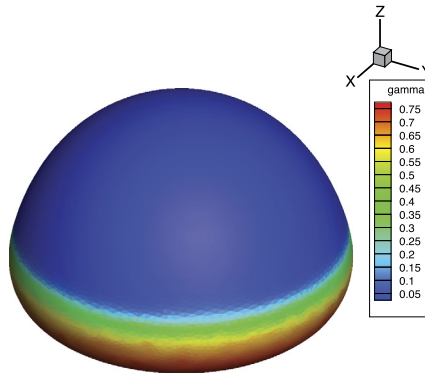


Fig. 11. Distribution of surface concentration on a buoyancy-driven contaminated bubble in an ellipsoidal regime. ($Eo = 10$, $Mo = 0.001$, $Pe_s = Pe_c = 1000$, $k = 1$, $Da = 10$, $Bi = 0.075$ and $D_h/d_b = 2.5$).

migration of a non-deformable bubble in an unbounded linear shear flow. They found that the surfactant can alter the lift force drastically.

Here we perform simulations to examine the effects of soluble surfactant on the lateral migration of a bubble in a pressure-driven channel flow. We consider a vertical channel as sketched in Fig. 12. The flow is driven by an applied pressure gradient $-\frac{dp}{dz}$ in the vertical (z) direction. No-slip boundary conditions are applied on the walls in the y direction while periodic boundary conditions are used in the other directions. The flow is initialized assuming a fully developed channel flow. A spherical bubble of diameter d_b is placed instantly near the left wall as shown in Fig. 12. The bubble is assumed to be clean initially and the bulk surfactant concentration is uniform at $C = C_\infty$. Assuming a fully developed channel flow, the average channel velocity is computed as

$$U_c = \frac{1}{12\mu_o} \left(-\frac{dp}{dz} \right) H^2$$

where H is the channel width. The computational domain is $5.23d_b \times 6.67d_b \times 10.48d_b$ in x , y and z directions, respectively. The center of the bubble is initially located at $(x_c, y_c, z_c) = (2.615d_b, 1.29d_b, 1.38d_b)$. The Reynolds numbers based of the bubble diameter and channel width are set to $Re_b = \frac{\rho_o U_c d_b}{\mu_o} = 150$ and $Re_c = \frac{\rho_o U_c H}{\mu_o} = 1000$, respectively. The other non-dimensional parameters are specified as $Pe_s = Pe_c = 250$, $Bi = 0.3$, $Da = 1.667$, $k = 0.4$, $\mu_i/\mu_o = 0.1$, $\rho_i/\rho_o = 0.1$ and $\beta_s = 0.5$ where the bubble diameter d_b and the average channel velocity U_c are used as the length and velocity scales, respectively. Deformability of the bubble is characterized by the capillary number defined as $Ca = \mu_o U_c / \sigma_s$. Computations are performed for capillary numbers $Ca = 0.05, 0.1$ and 0.2 for the clean and contaminated cases, to examine the combined effects of deformability and surfactant on the lateral migration of the bubbles. The corresponding Weber ($We = \rho_o U_c^2 d_c / \sigma_s$) and Eötvös ($Eo = g \Delta \rho d_c^2 / \sigma_s$) numbers are $(We, Eo) = (7.5, 0.81)$, $(15, 1.62)$ and $(30, 3.24)$. The domain is resolved by a $128 \times 192 \times 256$ grid that is slightly stretched near the walls in the y direction. The average distance from the wall (y_w) is called the separation distance and defined as the distance between the wall and the bubble center as shown in Fig. 12. The

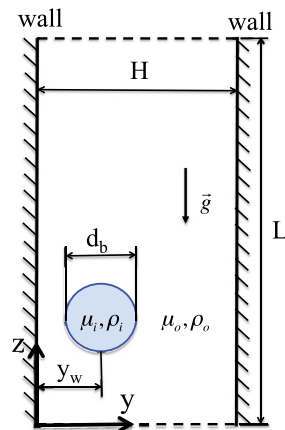


Fig. 12. Sketch for the pressure-driven flow.

average distance from the wall, the bubble terminal velocity in the axial direction and the bubble deformation are plotted in Fig. 13 as a function of time for the clean and contaminated cases. The separation distance is also plotted as a function of the axial distance (z_c) in the same figure. This figure shows that the clean bubble moves toward the wall due to the shear-induced lift force for all three capillary numbers and reaches a steady state with a certain distance from the wall, depending on the bubble deformability, i.e., the steady state separation distance increases with the capillary number. In the contaminated bubble case, the Marangoni stresses counteract the shear-induced lift force making the steady separation distance larger than the corresponding clean bubble case, in general, and eventually reverse the direction of the lateral migration completely for $Ca = 0.2$. The terminal velocity of contaminated bubble is larger than that of the clean bubble in all cases, mainly because the contaminated bubble moves closer to the channel center where the flow velocity is larger. Bubble deformation is also increased in the contaminated case except for $Ca = 0.2$ for which the bubble moves toward the channel center where shear is reduced. Fig. 14 shows the constant contours of the interfacial surfactant concentration at $t^* = 23.4$ for $Ca = 0.05$ and at $t^* = 49.8$ for $Ca = 0.2$ cases. As can be seen, the surfactant distribution is not axisymmetric in the less deformable case (i.e., $Ca = 0.05$) and minimum concentration is on the side facing the wall. Thus the net force induced by the Marangoni stresses is toward the channel center. For the more deformable case, the bubble moves to the channel centerline and thus the surfactant distribution becomes more axisymmetric. The evolution of interfacial surfactant concentration is illustrated in Fig. 15 for the most deformable case of $Ca = 0.2$. This figure shows that the interfacial surfactant concentration is non-axisymmetric at early times when the bubble is close to the wall and becomes more axisymmetric as it moves toward the channel centerline.

Finally the grid convergence of the method is demonstrated. For this purpose, computations are performed for the $Ca = 0.2$ and $Ca = 0.1$ cases using various grid resolutions ranging between $64 \times 96 \times 128$ and $256 \times 384 \times 512$. The top plots in Fig. 16 show the separation distance computed using these grid resolutions for $Ca = 0.2$ and $Ca = 0.1$. In both cases, the difference between the successive grid resolutions decreases, indicating grid convergence. In the case of $Ca = 0.1$, the difference between results obtained on the $128 \times 192 \times 256$ and the $256 \times 384 \times 512$ grids is relatively large since this case is in the transition regime so it is more difficult to compute. The bottom plots in Fig. 16 show the separation distance plotted against the square of the normalized grid size at the times marked with vertical dotted lines in the top plots. The nearly linear relation confirms the expected second order accuracy of the method. Finally the constant contours of the interfacial surfactant concentration computed on the $128 \times 192 \times 256$ and the $256 \times 384 \times 512$ grids are plotted in Fig. 17 to visually demonstrate the grid convergence.

6. Conclusions

A finite-difference/front-tracking method is developed for simulations of soluble surfactants in 3D multiphase flows. The interfacial and bulk surfactant concentration evolution equations are solved fully coupled with the incompressible Navier-Stokes equations. A non-linear equation of state is used to relate interfacial surface tension to surfactant concentration at the interface. The method can accommodate virtually any equation of state available in the literature. The numerical algorithm is implemented in parallel using a domain decomposition method. The message passing interface (MPI) library is used for communication between processors. In the present implementation, the surfactant is assumed to be contained in the ambient fluid but it is very straightforward to extend the method to simulate cases where the surfactant is contained in the drop phase or created at the interface as a result of a chemical reaction between the solutes in the drop and bulk fluids.

The method is validated for simple test cases and the computational results are found to be in a good agreement with the analytical or numerical solutions. The method is then applied to study the effects of soluble surfactants on the motion of buoyancy-driven bubbles in a straight square channel in nearly undeformable (spherical) and deformable (ellipsoidal) regimes. The retardation effect of the surfactant is demonstrated for these cases. A stagnant-cap like distribution of inter-

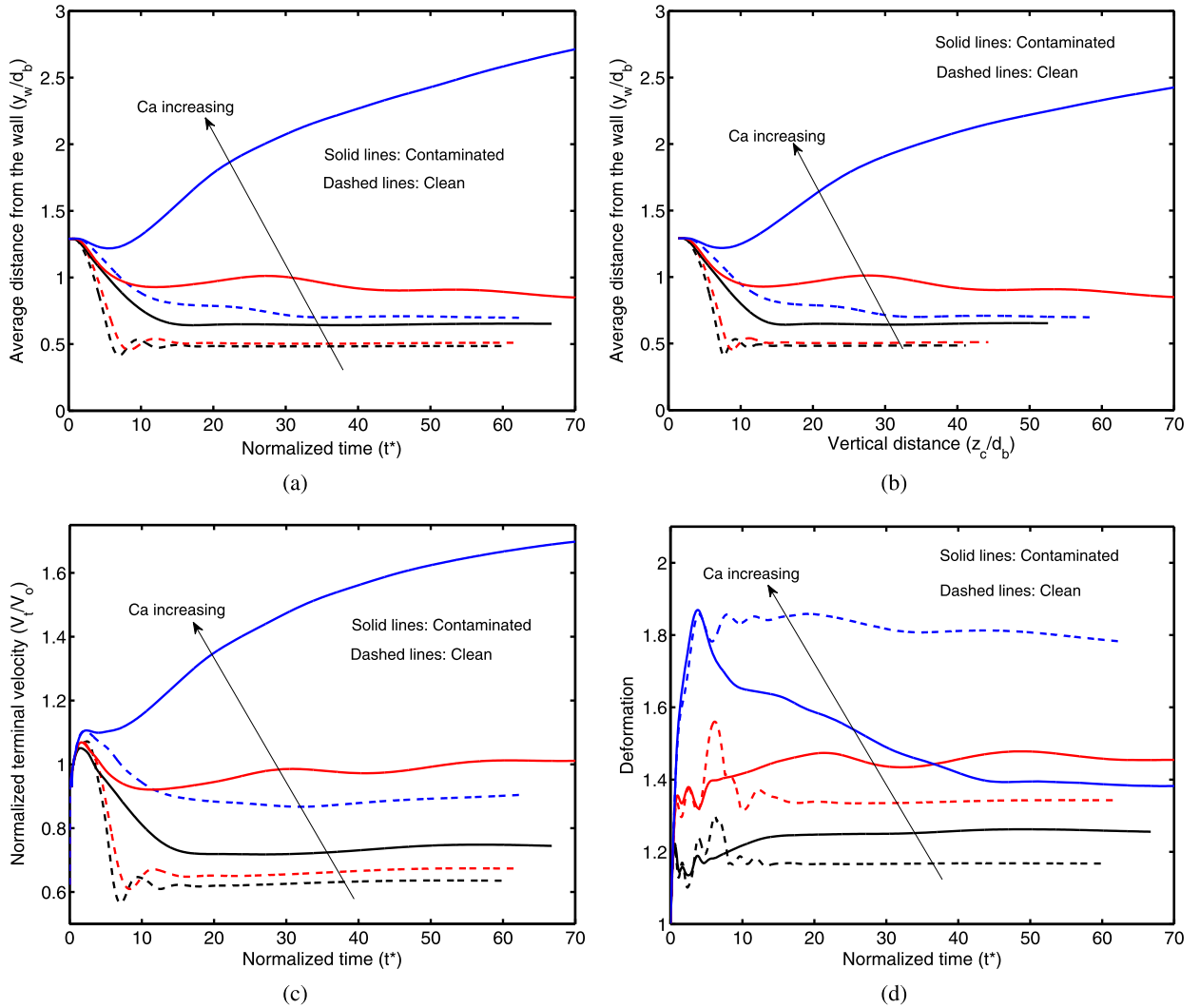


Fig. 13. Pressure driven flow: The time evolution of (a) the average distance from the wall, (c) the terminal velocity and (d) the deformation of the bubble. (b) The average distance from the wall versus the axial location of the bubble centroid. The results are obtained for $Ca = 0.05, 0.1$ and 0.2 . ($Re_c = 1000$, $Re_b = 150$, $Pe_s = Pe_c = 250$, $Bi = 0.3$, $Da = 1.667$, $k = 0.4$ and $\beta_s = 0.5$).

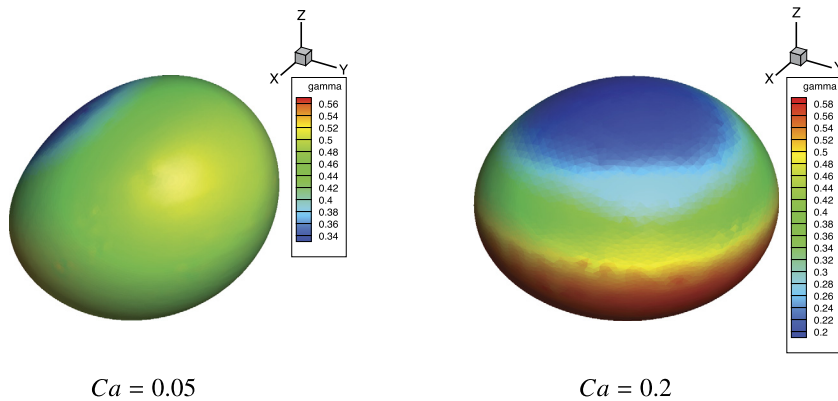


Fig. 14. Surface concentration for $Ca = 0.05$ at $t^* = 23.4$ and for $Ca = 0.2$ at $t^* = 49.8$. The other parameters are $Re_c = 1000$, $Re_b = 150$, $Pe_s = Pe_c = 250$, $Bi = 0.3$, $Da = 1.667$, $k = 0.4$ and $\beta_s = 0.5$.

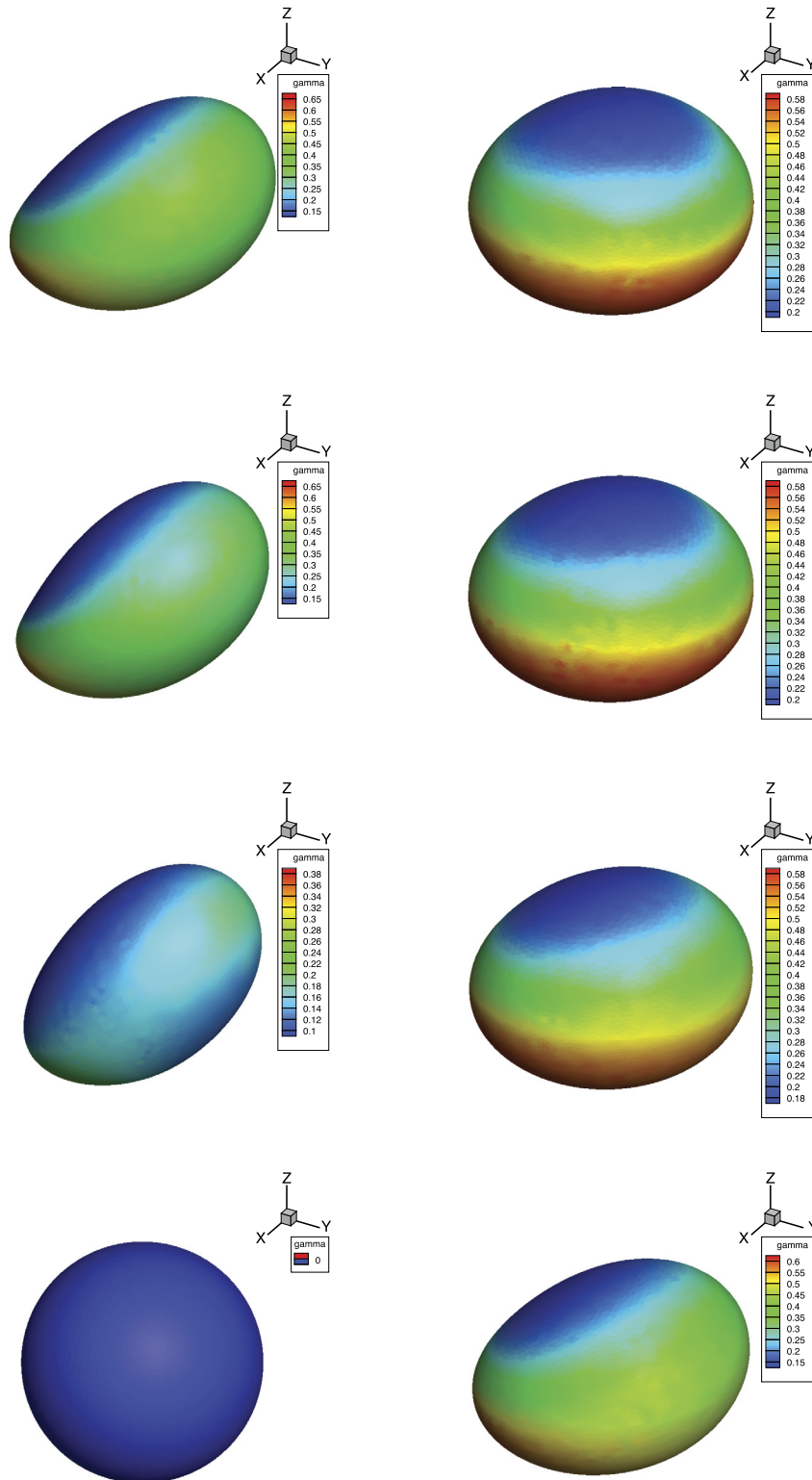


Fig. 15. Evolution of contaminated droplet in the pressure-driven flow for $Ca = 0.2$ as it moves away from the wall. Time evolves from bottom to top and from left to right. The snapshots are taken at times $t^* = 0, 1.67, 11.67, 21.67, 35.0, 68.33, 101.67, 135.0$. The other parameters are $Re_c = 1000, Re_b = 150, Pe_s = Pe_c = 250, Bi = 0.3, Da = 1.667, k = 0.4$ and $\beta_s = 0.5$.

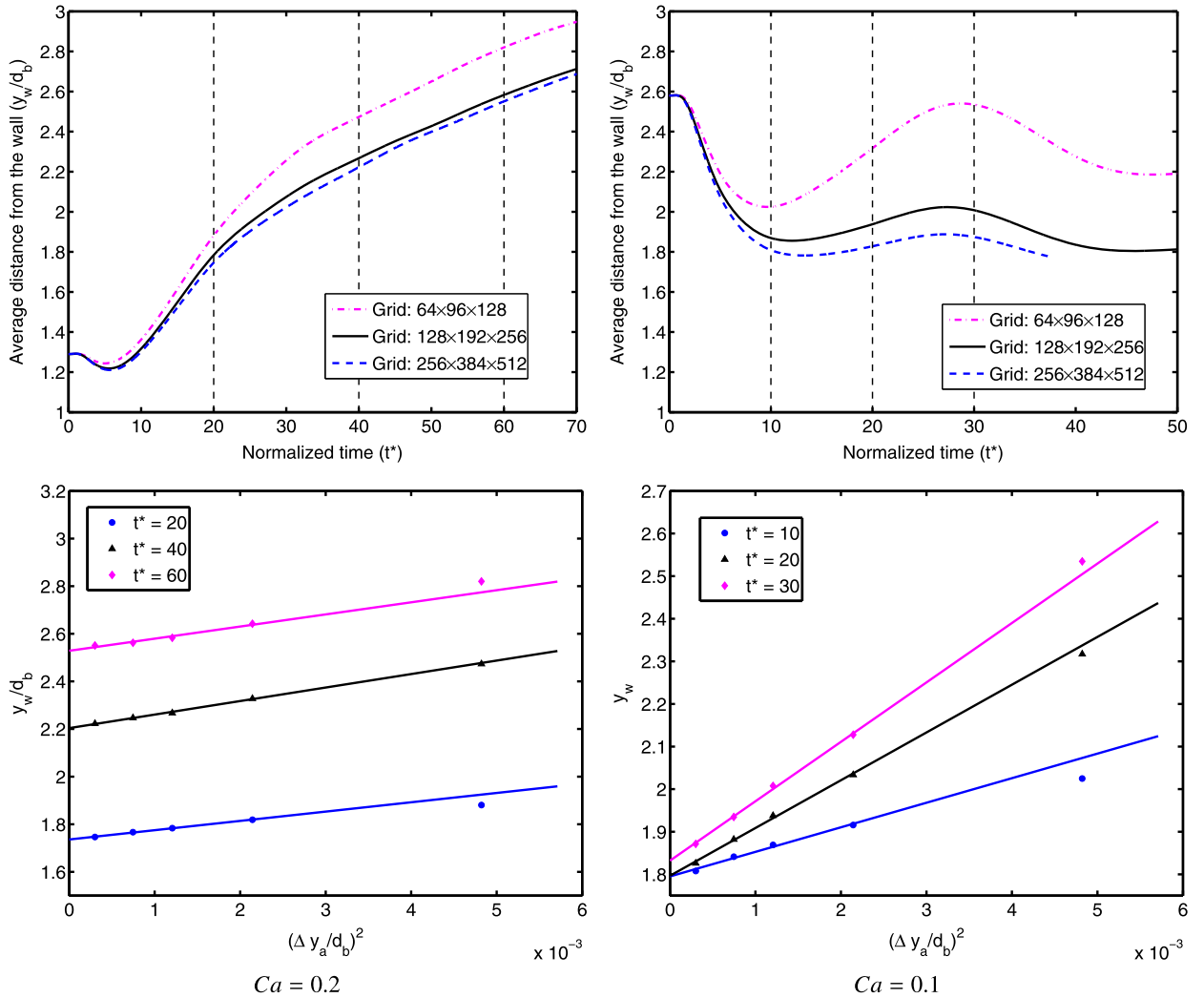


Fig. 16. Top plots: Variation of normalized distance from the wall as a function of non-dimensional time computed with $64 \times 96 \times 128$, $128 \times 192 \times 256$ and $256 \times 384 \times 512$ grids. Bottom plots: The normalized distance from the wall against the square of the normalized grid size at the times marked with the vertical dashed lines in the top plots. ($Re_c = 1000$, $Re_b = 150$, $Pe_s = Pe_c = 250$, $Bi = 0.3$, $Da = 1.667$, $k = 0.4$ and $\beta_s = 0.5$).

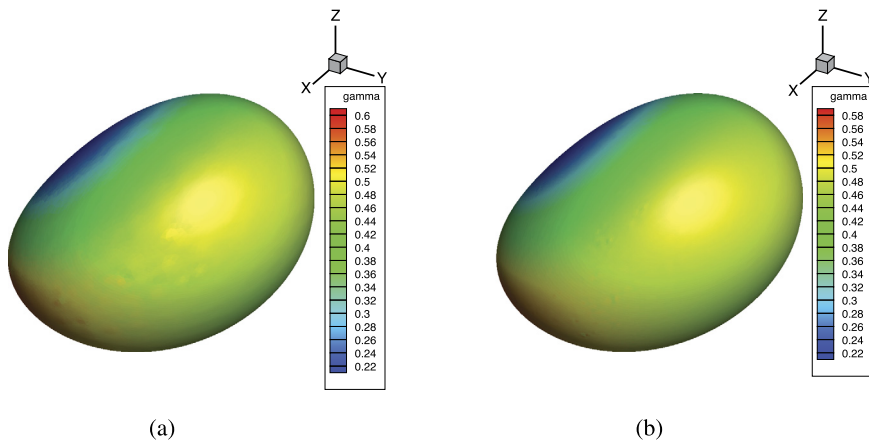


Fig. 17. Grid convergence: (a) Coarse grid containing $128 \times 192 \times 256$ cells. (b) Fine grid containing $256 \times 384 \times 512$ cells. ($Ca = 0.1$, $Re_c = 1000$, $Re_b = 150$, $Pe_s = Pe_c = 250$, $Bi = 0.3$, $Da = 1.667$, $k = 0.4$ and $\beta_s = 0.5$).

facial surfactant concentration is observed in the ellipsoidal regime. Finally the method is used to examine the effects of soluble surfactants on the lateral migration of bubbles in a pressure-driven channel flow. It is found that surfactant induced Marangoni stresses counteract the shear-induced lift force making the steady separation distance larger than for the corresponding clean bubble case and eventually reverse the direction of the lateral bubble migration completely when the capillary number exceeds a critical value.

The grid convergence of the method has been demonstrated using the pressure-driven channel flow case and it is found that the method is second order accurate in space.

Future work includes development of a multi-scale method for efficient computations of soluble surfactants in 3D multiphase flows containing thin mass boundary layers, i.e., at high Peclet numbers, following the methodology proposed by Aboulhasanzadeh et al. [1,2].

Acknowledgements

The first author (MM) is supported by the Scientific and Technical Research Council of Turkey (TUBITAK), Grant 112M181 and Turkish Academy of Sciences (TUBA). We thank Charles de Langavant for bringing the error in the analytical solution given by Eq. (52) to our attention.

References

- [1] B. Aboulhasanzadeh, S. Thomas, M. Taeibi-Rahni, G. Tryggvason, Multiscale computations of mass transfer from buoyant bubbles, *Chem. Eng. Sci.* 75 (2012) 456.
- [2] B. Aboulhasanzadeh, S. Hosoda, A. Tomiyama, G. Tryggvason, A validation of an embedded analytical description approach for the computations of high Schmidt number mass transfer from bubbles in liquids, *Chem. Eng. Sci.* 101 (2013) 165.
- [3] S. Adami, X. Hu, N. Adams, A conservative SPH method for surfactant dynamics, *J. Comput. Phys.* 229 (2010) 1909.
- [4] S.L. Anna, H.C. Meyer, Microscale tip streaming in a microfluidic flow focusing device, *Phys. Fluids* 18 (12) (2006) 121512.
- [5] I.B. Bazhlekov, P.D. Anderson, H.E.H. Meijer, Numerical investigation of the effect of insoluble surfactants on drop deformation and breakup in simple shear flow, *J. Colloid Interface Sci.* 298 (1992) 369.
- [6] M.R. Booty, M. Siegel, A hybrid numerical method for interfacial fluid flow with soluble surfactant, *J. Comput. Phys.* 229 (2010) 3864.
- [7] R. Borges, M. Carmona, B. Costa, W. Don, An improved weighted essentially non-oscillatory scheme for hyperbolic conservation laws, *J. Comput. Phys.* 227 (2008) 3191.
- [8] A.R. Chorin, Numerical solution of the Navier–Stokes equations, *Math. Comput.* 22 (1968) 745.
- [9] R. Clift, J.R. Grace, M.E. Weber, *Bubbles, Drops and Particles*, Dover, 2005.
- [10] S. Dabiri, J. Lu, G. Tryggvason, Transition between regimes of a vertical channel bubbly upflow due to bubble deformability, *Phys. Fluids* 25 (2013) 102110.
- [11] M.A. Drumright-Clarke, Y. Renardy, The effect of insoluble surfactant at dilute concentration on drop breakup under shear with inertia, *Phys. Fluids* 16 (1) (2004) 14.
- [12] C.D. Eggleton, K.J. Stebe, An adsorption–desorption controlled surfactant on a deforming droplet, *J. Colloid Interface Sci.* 208 (1998) 68.
- [13] C.D. Eggleton, T.M. Tsai, K.J. Stebe, Tip-streaming from a drop in the presence of surfactants, *Phys. Rev. Lett.* 87 (2001) 048302.
- [14] R. Falgout, A. Baker, E. Chow, V.E. Henson, E. Hill, J. Jones, T. Kolev, B. Lee, J. Painter, C. Tong, P. Vassilevski, U.M. Yang, Users manual, HYPRE high performance preconditioners, <http://www.llnl.gov/CASC/hypre/>.
- [15] H. Fujioka, A continuum model of interfacial surfactant for particle methods, *J. Comput. Phys.* 234 (2013) 280.
- [16] M. Fukuta, S. Takagi, Y. Matsumoto, Numerical study on the shear-induced lift force acting on a spherical bubble in aqueous surfactant solutions, *Phys. Fluids* 20 (2008) 040704.
- [17] S. Ganesan, L. Tobiska, A coupled arbitrary Lagrangian–Eulerian and Lagrangian method for computation of free surface flows with insoluble surfactants, *J. Comput. Phys.* 228 (8) (2009) 2859.
- [18] S. Ganesan, L. Tobiska, Arbitrary Lagrangian–Eulerian finite-element method for computation of two-phase flows with soluble surfactant, *J. Comput. Phys.* 231 (2012) 3685.
- [19] J. Grotberg, Respiratory fluid mechanics and transport processes, *Annu. Rev. Biomed. Eng.* 3 (2001) 421.
- [20] A.K. Henrick, T.D. Aslam, J.M. Powers, Mapped weighted essentially non-oscillatory schemes: achieving optimal order near critical points, *J. Comput. Phys.* 207 (2005) 542.
- [21] A.J. James, J. Lowengrub, A surfactant-conserving volume-of-fluid method for interfacial flows with insoluble surfactants, *J. Comput. Phys.* 201 (2004) 685.
- [22] G.-S. Jiang, C.-W. Shu, Efficient implementation of weighted ENO schemes, *J. Comput. Phys.* 126 (1996) 202.
- [23] F. Jin, N.R. Gupta, K.J. Stebe, The detachment of a viscous drop in a viscous solution in the presence of a soluble surfactant, *Phys. Fluids* 18 (2006) 022103.
- [24] R.A. Johnson, A. Borhan, Pressure-driven motion of surfactant-laden drops through cylindrical capillaries: effect of surfactant solubility, *J. Colloid Interface Sci.* 261 (2003) 529.
- [25] A.H. Jorbe, Drug-therapy – pulmonary surfactant therapy, *N. Engl. J. Med.* 328 (1993) 861.
- [26] S. Khatri, A.-K. Tornberg, An embedded boundary method for soluble surfactant with interface tracking for two-phase flows, *J. Comput. Phys.* 256 (2014) 768.
- [27] S. Khatri, A.-K. Tornberg, A numerical method for two phase flows with insoluble surfactants, *Comput. Fluids* 49 (1) (2011) 150.
- [28] M.-C. Lai, Y.-H. Tseng, H. Huang, An immersed boundary method for interfacial flows with insoluble surfactant, *J. Comput. Phys.* 227 (2008) 7279.
- [29] C. de Langavant, Private communication, 2013.
- [30] B.P. Leonard, A stable and accurate convective modelling procedure based on quadratic upstream interpolation, *Comput. Methods Appl. Mech. Eng.* 19 (1) (1979) 59.
- [31] X.F. Li, C. Pozrikidis, The effect of surfactants on drop deformation and on the rheology of dilute emulsions in Stokes flow, *J. Fluid Mech.* 341 (1997) 165.
- [32] V.G. Levich, *Physicochemical Hydrodynamics*, Prentice Hall, 1962.
- [33] H. Liu, Y. Zhang, Phase-field modeling droplet dynamics with soluble surfactant, *J. Comput. Phys.* 229 (2010) 9166.
- [34] J. Lu, G. Tryggvason, Effect of bubble deformability in turbulent bubbly upflow in a vertical channel, *Phys. Fluids* 20 (2008) 0407010.

- [35] J. Lu, G. Tryggvason, Dynamics of nearly spherical bubbles in a turbulent channel upflow, *J. Fluid Mech.* 732 (2013) 732, 166.
- [36] W.J. Milleken, H.A. Stone, L.G. Leal, The effect of surfactant on transient motion of newtonian drops, *Phys. Fluids A* 5 (1993) 69.
- [37] W.J. Milleken, L.G. Leal, The influence of surfactant on the deformation and breakup of a viscous drop – the effect of surfactant solubility, *J. Colloid Interface Sci.* 166 (1994) 275.
- [38] M. Muradoglu, G. Tryggvason, A front-tracking method for computation of interfacial flows with soluble surfactants, *J. Comput. Phys.* 227 (4) (2008) 2238.
- [39] U. Olgac, M. Muradoglu, Computational modeling of unsteady surfactant-laden liquid plug propagation in neonatal airways, *Phys. Fluids* 25 (2013) 071901.
- [40] U. Olgac, M. Muradoglu, Effects of surfactant on liquid film thickness in the Bretherton problem, *Int. J. Multiph. Flow* 48 (2013) 58.
- [41] C. Pozrikidis, Interfacial dynamics for Stokes flow, *J. Comput. Phys.* 169 (2001) 250.
- [42] C. Pozrikidis, A finite-element method for interfacial surfactant transport with applications to the flow-induced deformation of a viscous drop, *J. Eng. Math.* 49 (2004) 163.
- [43] R.F. Probstein, *Physicochemical Hydrodynamics: An introduction*, John Wiley & Sons, Inc., Hoboken, NJ, 2003.
- [44] J. Sjoblom (Ed.), *Emulsions and Emulsion Stability*, Taylor & Francis, London, UK, 2005.
- [45] H.A. Stone, A.D. Stroock, A. Ajdari, Engineering flows in small devices: microfluidics toward lab-on-a-chip, *Annu. Rev. Fluid Mech.* 36 (2004) 381.
- [46] H.A. Stone, Dynamics of drop deformation and breakup in viscous fluids, *Annu. Rev. Fluid Mech.* 26 (1994) 65.
- [47] H.A. Stone, A simple derivation of the time-dependent convective–diffusion equation for surfactant transport along a deforming interface, *Phys. Fluids A* 2 (1990) 111.
- [48] H.A. Stone, L.G. Leal, The effects of surfactants on drop deformation and breakup, *J. Fluid Mech.* 220 (1989) 161.
- [49] T.N. Swaminathan, K. Mukundakrishnan, P.S. Ayyaswamy, D.M. Eckmann, Effect of a soluble surfactant on a finite-sized bubble motion in a blood vessel, *J. Fluid Mech.* 642 (2010) 509.
- [50] P. Tabeling, *Introduction to Microfluidics*, Oxford University Press, Oxford, UK, 2010.
- [51] S. Takagi, T. Ogasawara, Y. Matsumoto, The effects of surfactant on the multiscale structure of bubbly flows, *Philos. Trans. R. Soc. Lond. A* 366 (2008) 2117.
- [52] S. Takagi, Y. Matsumoto, Surfactant effects on bubble motion and bubbly flows, *Annu. Rev. Fluid Mech.* 43 (2011) 615.
- [53] S. Tasoglu, U. Demirci, M. Muradoglu, The effect of soluble surfactant on the transient motion of a buoyancy-driven bubble, *Phys. Fluids* 20 (2008) 040805.
- [54] K.E. Teigen, P. Song, J. Lowengrub, A. Voigt, A diffuse-interface method for two-phase flows with soluble surfactants, *J. Comput. Phys.* 230 (2011) 375.
- [55] G. Tryggvason, B. Bunner, A. Esmaeeli, D. Juric, N. Al-Rawahi, W. Tauber, J. Han, S. Nas, Y.-J. Jan, A front-tracking method for the computations of multiphase flow, *J. Comput. Phys.* 169 (2) (2001) 708.
- [56] G. Tryggvason, R. Scardovelli, S. Zaleski, *Direct Numerical Simulations of Gas–Liquid Multiphase Flows*, Cambridge University Press, Cambridge, UK, 2011.
- [57] T.M. Tsai, M.J. Miksis, The effects of surfactant on the dynamics of bubble snap-off, *J. Fluid Mech.* 337 (1997) 381.
- [58] S.O. Unverdi, G. Tryggvason, A front-tracking method for viscous incompressible multiphase flows, *J. Comput. Phys.* 100 (1992) 25.
- [59] C.E. Weatherburn, *Differential Geometry of Three Dimensions*, vol. I, Cambridge University Press, Cambridge, UK, 1927.
- [60] J.-J. Xu, Z. Li, J. Lowengrub, H. Zhao, A level-set method for interfacial flows with surfactant, *J. Comput. Phys.* 212 (2006) 590.
- [61] J.-J. Xu, Y. Yang, J. Lowengrub, A level-set continuum method for two-phase flows with insoluble surfactant, *J. Comput. Phys.* 231 (2012) 5897.
- [62] N.O. Young, J.S. Goldstein, M.J. Block, The motion of bubbles in a vertical temperature gradient, *J. Fluid Mech.* 6 (1959) 350.
- [63] J. Zhang, D.M. Eckmann, P.S. Ayyaswamy, A front tracking method for a deformable intravascular bubble in a tube with soluble surfactant transport, *J. Comput. Phys.* 214 (1) (2006) 366.